Phase-field guided design of record-high piezoelectricity and discovery of simultaneous high light-transparency and high piezoelectricity in relaxor ferroelectrics

Fei Li[1], Bo Wang[2], Long-Qing Chen[3]

[1]Electronic Materials Research Lab, Key Lab of Education Ministry, School of Electronic Science and Engineering, Xi'an Jiaotong University, Xi'an, 710049, China

[2]Materials Science Division, Lawrence Livermore National Laboratory, Livermore CA, 94550, USA

[3]Materials Research Institute and Materials Science and Engineering, Pennsylvania State University, University Park, PA, 16802, USA

The phase-field method has been extensively applied to predicting the domain structures and their responses to external fields and understanding experimentally observed domain states under different electromechanical conditions in ferroelectric heterostructures. This article highlights the successful examples of phase-field applications in guiding the design of relaxor-ferroelectric ceramics and crystals with record-high piezoelectricity and the discovery of simultaneous high light-transparency and piezoelectricity of relaxor-ferroelectric crystals for a wide range of biomedical, robotics, and optoelectronics applications.

Keywords: Ferroelectric; Piezoelectric; Phase-field simulations; Relaxor ferroelectrics

Introduction

The discovery of relaxor-ferroelectric solid-solution single crystals (relaxor-PT), such as $Pb(Mg_{1/3}Nb_{2/3})O_3$-$PbTiO_3$ (PMN-PT) and $Pb(Zn_{1/3}Nb_{2/3})O_3$-$PbTiO_3$ (PZN-PT), is considered to be a milestone achievement in the fields of ferroelectric and piezoelectric materials. The first growth of relaxor-PT crystals was around late 1960s by Soviet and Japanese researchers[1, 2] while the high piezoelectricity (piezoelectric coefficient d_{33}~1200 pC/N) in relaxor-PT crystals was first reported in early 1980s by Kuwata J et al.[3] Although relaxor-PT crystals were believed to possess high piezoelectric coefficient, there are several critical issues in their single crystal growth, such as composition segregation and incongruent melting of various oxides (e.g., TiO_2, MgO, ZnO, Nb_2O_5). As a result, the crystal qualities were not sufficiently high, and the crystal sizes were too small (several millimeters) to systematically characterize their properties or to be deployed in piezoelectric devices with sufficient durability. In 1990s, a milestone was achieved by Shrout and co-workers who successfully grew high-quality PZN-PT crystals with ultrahigh piezoelectric coefficient d_{33} of 2500 pC/N, electromechanical coupling factor of 95%, and electric-field-induced strain of ~1.5%,[4] which generated considerable attention from both academia and industry and encouraged extensive efforts

to further improve the crystal growth techniques, understand the origin of high piezoelectricity, optimize the piezoelectric property, and explore their use in devices.[5-16]

However, despite extensive efforts to enhance the piezoelectricity of relaxor-PT driven by the ever-increasing demands of advanced piezoelectric devices, there have been no breakthroughs[16] during the past two decades to drastically enhance piezoelectricity until very recently.[17-20] The present article highlights the important roles of phase-field simulations in understanding the roles of nanoscale heterogeneous polar regions in determining the piezoelectric activity of relaxor-PT crystals[21, 22] as well as in guiding the design of relaxor-PT ceramics and single crystals with record-high piezoelectricity through rare-earth element doping[17, 18] and the discovery of simultaneous high light-transparency and piezoelectricity through alternating current (a.c.) electric field poling.[23-25] Both the rare-earth-doped ceramics and single crystals and the transparent PMN-PT and PIN-PMN-PT piezoelectric crystals are now being actively explored and implemented in various device applications[26-31].

A brief description on phase-field method of ferroelectrics

In the phase-field method of ferroelectrics, the spontaneous polarization is the natural internal process order parameter for describing the ferroelectric phase transitions, domain structures, and responses to external electrical and mechanical fields (see Ref. 32-34). The total free energy of an inhomogeneous ferroelectric crystal includes contributions from the local chemical energy density and the energy due to the local polarization gradient, electrostatic energy, and elastic strain energy. The fundamental equation of thermodynamics for a ferroelectric crystal automatically takes into account the couplings between the local polarization, mechanical strain/stress, and electric field. The thermodynamic parameters of a phase-field model are usually obtained using a combination of experimentally measured temperature-dependent structural and physical properties (e.g., temperature-dependent lattice parameters, dielectric and piezoelectric properties, and the phase transition temperatures) and computed relative energies of polarization states from first-principles atomistic calculations. The different polarization, mechanical, and electric boundary conditions can be employed to model the ferroelectric bulk single crystals, polycrystals, as well as nanoscale thin films and heterostructures. The solutions to the time-dependent Ginzburg-Landau relaxation equations or Klein-Gordon dynamic equations for the evolution of polarization describe the domain structure evolution of ferroelectric materials as well as the linear and nonlinear electromechanical responses.

Design record-high piezoelectricity in relaxor-PT ceramics and crystals

We start with the attempt to understand the impacts of nanoscale heterogeneous polar regions on piezoelectricity through phase-field simulations. A distinct microstructural feature of relaxor-PTs compared to classical ferroelectrics is the presence of nanoscale heterogeneous polar regions within ferroelectric domains resulting from cation order-disorder and the accompanied random fields/bonds.[35-37] A common approach for evaluating the contribution of nanoscale heterogeneous polar regions is to analyze the dielectric response with respect to frequency and temperature. The contribution of nanoscale heterogeneous polar regions to dielectric permittivity can be eliminated at the frequencies above their relaxation frequencies or at the temperatures below their "frozen" temperatures. In addition, to eliminate the influence related to ferroelectric domain walls, single-domain relaxor-PT crystals should be utilized.[21] **Fig. 1a** and **b** show the temperature and frequency dependent dielectric behavior for a single domain PZN-0.15PT crystal. Strong dispersion of the permittivity is seen only at cryogenic temperature (dashed circle in Fig. 1a). The variation of the piezoelectric coefficient below room temperature is parallel to that of the dielectric permittivity since the piezoelectric coefficient of a single domain ferroelectric crystal is proportional to the product of spontaneous polarization, electrostrictive coefficient and dielectric permittivity, and the variations of spontaneous polarization and electrostrictive coefficient with temperature are minimal compared to that of the dielectric permittivity below room temperature. Fig. 1c is a schematic showing the high room-temperature dielectric and piezoelectric properties of relaxor-PT crystals compared to classical ferroelectric crystals, which can be attributed to a *thermal activation* process around 100 K. Thus, elucidating the mechanism(s) responsible for the dielectric/piezoelectric variation at cryogenic temperatures is critical to understanding the ultrahigh piezoelectric properties of relaxor–PT crystals at room temperature.

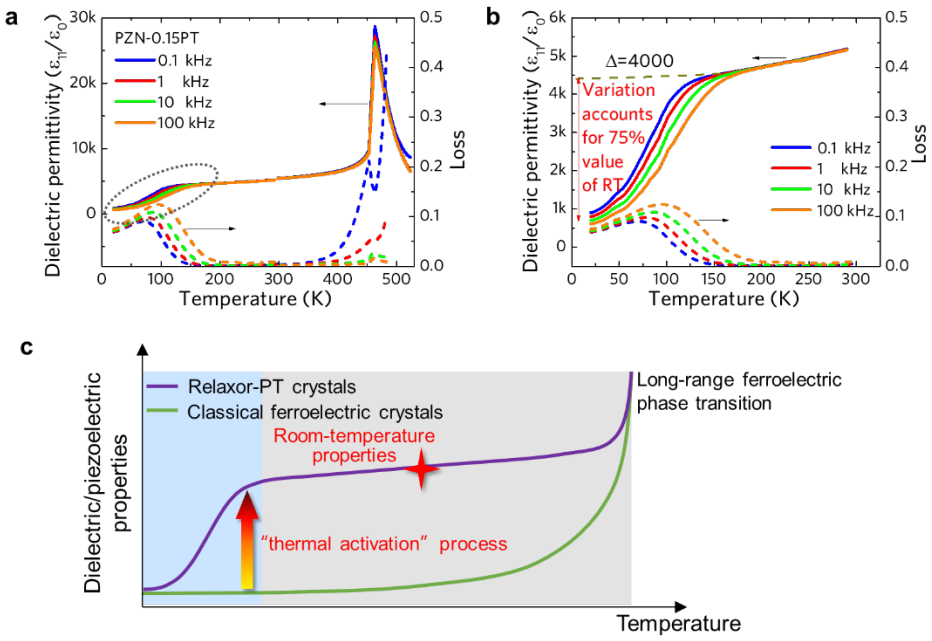

Figure 1 (a) The dielectric permittivity as a function of temperature for PZN–0.15PT crystal measured as different frequencies. A tetragonal–cubic phase transition exists at 468 K. (b) Enlarged low-temperature sections (20–300 K) for (a). (c) A schematic plot showing the major difference in dielectric/piezoelectric properties between relaxor–PT crystals and classical ferroelectric crystals. The data are from reference 21.

We performed phase-field simulations to obtain the dielectric variation at cryogenic temperature. We consider a single tetragonal domain (the long-range ferroelectric phase of PZN-0.15PT) containing local polar regions, as shown in **Fig. 2**, in an orthorhombic polar state[21]. The simulations successfully reproduced the temperature dependence of the dielectric properties of PZN-0.15PT crystal (**Fig. 3a**). The observed *thermal activation* process of dielectric permittivity was associated with the energies arising from the nanoscale structural heterogeneity.

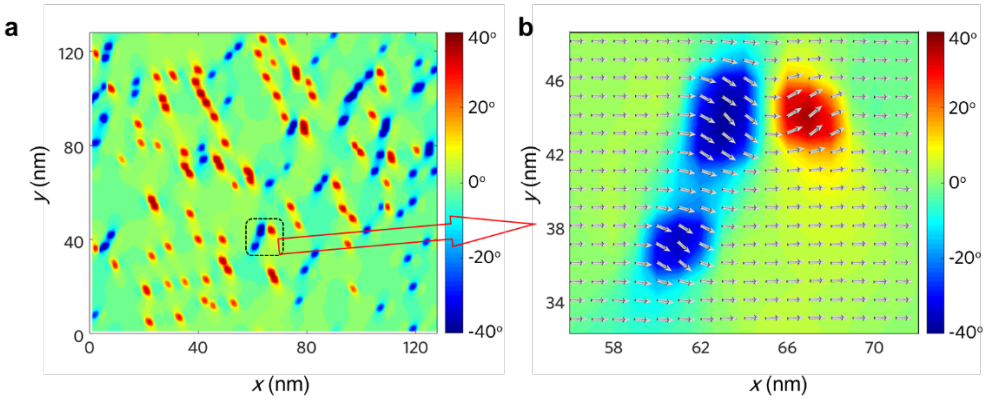

Figure 2 (a) Phase-field-simulated microstructures for a [100]-poled single domain PZN-0.15PT crystal at 100 K. (b) The enlarged square area in (a), where the polar vectors of every grid are shown.

The *x* and *y* axes represent the [100] and [010] crystallographic directions, respectively. The color bar denotes the angle between the polar vector of the grids and the [100] direction. In this 2D simulation, the size of a single grid is 1×1 nm. The lattice parameter of PZN-0.15PT (pseudo-cubic phase) is ~0.4 nm. The data are from reference 21.

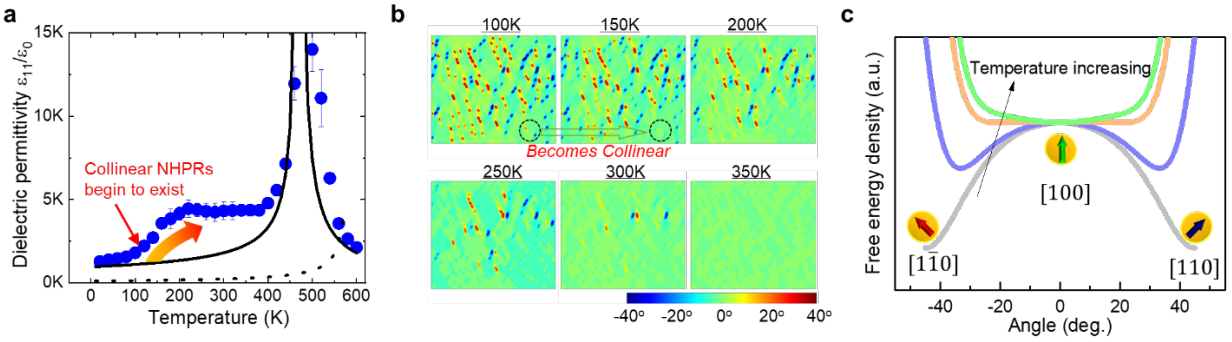

Figure 3 (a) The simulated dielectric permittivity of [100]-poled single domain PZN-0.15PT crystal as a function of temperature. (b) Temperature-dependent map of polarization vector direction for the [100]-poled single domain PZN-0.15PT crystal obtained by phase field simulation. The color bar denotes the angle between the polar vector of the grids and the [100] direction. (c) Schematic illustration of the transition of nanoscale heterogeneous polar regions to the 'collinear' state as the temperature increases from 100 to 150 K. NHPRs in (a) stand for nanoscale heterogeneous polar regions. (a-b) are from reference 21.

In the phase-field model of relaxor-PT crystals, the energies associated with local structural heterogeneity arising from the discontinuity of polarization and strain around the interfaces among tetragonal matrix and local polar regions (called as heterogeneity energies), including electrostatic, polarization gradient and elastic energies, provide the driving force for the transformation of those local regions to a tetragonal state, to reduce or eliminate the polarization discontinuity. As shown in Fig. 3b, with increasing the temperature the polar vectors of nanoscale heterogeneous polar regions transform to the [100] direction, i.e., become parallel with the polar direction of the tetragonal ferroelectric matrix. Meanwhile, the competition between the bulk and heterogeneity energies leads to a highly flattened free energy profile of nanoscale heterogeneous polar regions, as schematically shown in Fig. 3c. The polar vectors of aligned nanoscale heterogeneous polar regions are much easier to be rotated by an electric field compared to that of the ferroelectric matrix, leading to enhanced dielectric and piezoelectric properties, as shown in **Fig. 4**.

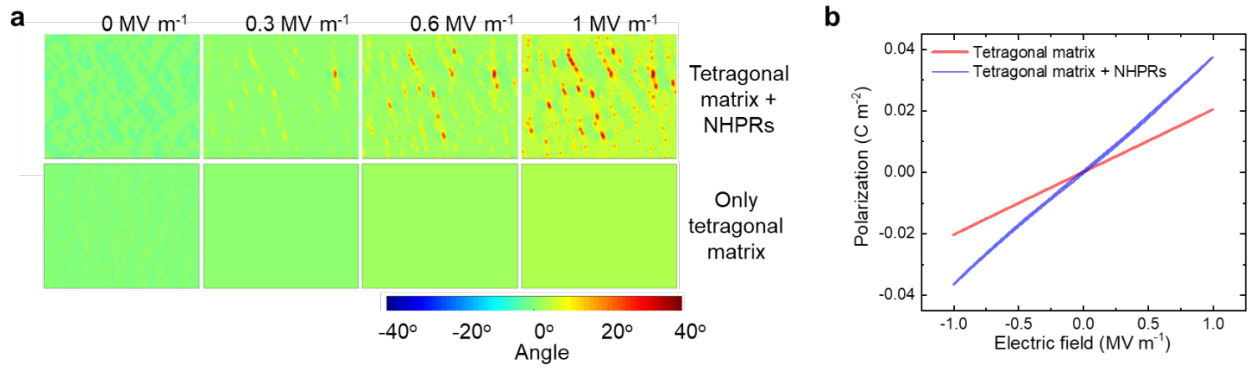

Figure 4 (a) Simulated microstructural variation under a transverse electric field (i.e., the electric field is perpendicular to the apparent polarization of the ferroelectric domain) for [100]-poled single domain PZN-0.15PT crystal at 350 K (note, without an electric field, all the regions are in tetragonal state at 350 K due to the impact of heterogeneity energies). For comparison, the same simulations were also performed on the tetragonal ferroelectric single domain without nanoscale heterogeneous polar regions. (b) Simulated transverse dielectric response of the heterogeneous ferroelectric system with comparison to a homogeneous ferroelectric system (i.e., tetragonal matrix only). NHPRs in (a,b) stand for nanoscale heterogeneous polar regions. A part of data in (a) is from reference 21.

The predicted temperature dependence of microstructural variation is confirmed by the neutron and X-ray diffraction results, i.e., the diffuse scattering became stronger from room temperature to cryogenic temperatures for relaxor-PTs.[38]

To enhance the piezoelectricity of relaxor-PTs, we performed further phase-field simulations and found out that the room-temperature dielectric permittivity can be enhanced by increasing the volume fraction of nanoscale heterogeneous polar regions in the heterogeneous system (Fig. 2), as shown in **Fig. 5a**. Furthermore, as shown in Fig. 5b, the system with a larger volume fraction of nanoscale heterogeneous polar regions corresponds to a higher loss maximum at cryogenic temperature.

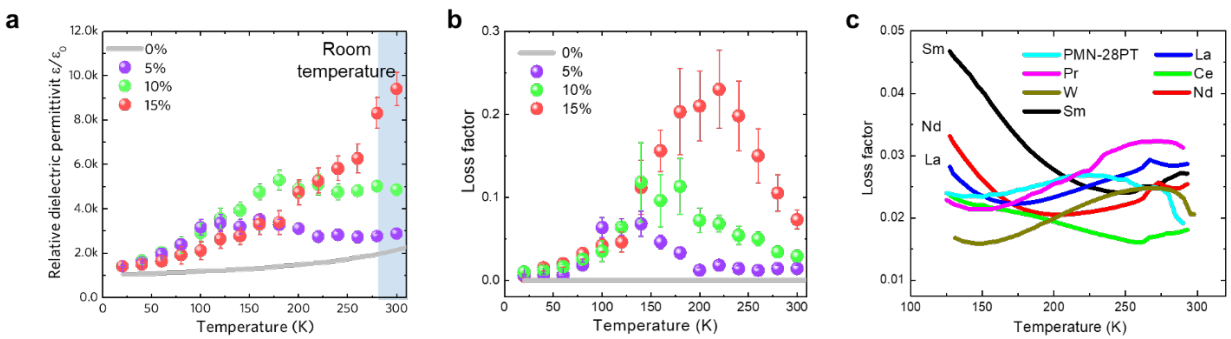

Figure 5 Phase-field simulation of the transverse dielectric permittivity (a) and loss factors (b) for the heterogeneous systems. The volume fraction of the heterogeneous regions varies from 0% to 15%.

(c) Temperature dependence of dielectric loss factors for PMN-28PT ceramics with different rare-earth dopants. The concentration of dopants is 2 mol%. The data were measured at 1 kHz. The data is from reference 18.

Following the phase-field simulation results, we performed experiments to increase the local structural heterogeneity of relaxors-PTs by doping rare-earth elements, since previous experiments indicated that rare-earth dopants can introduce effective random fields/bonds and/or change the ordering degree of B-site cations.[39] Hinted by the signature of dielectric loss obtained in phase-field simulations, we characterized low-temperature dielectric losses of rare-earth element doped PMN-PT ceramics to evaluate the impact of various rare-earth dopants on the local structural heterogeneity in PMN-PT.[18] Based on the amount of losses, we were able to identify rare-earth element Sm as the best candidate dopant to modify the local structure of PMN-PT since this system exhibits the highest loss factor at cryogenic temperatures compared to other doped PMN–PT systems, as shown in Fig. 5c. Remarkably, the Sm-doped PMN-PT ceramics achieved record-high piezoelectric responses among ceramics, and the piezoelectricity of the corresponding crystals nearly doubled the 20-year old record, as shown in **Fig. 6**.[17,18] These Sm-doped PMN-PT crystals and ceramics are of practical importance for high-performance electromechanical applications,[26-28] e.g., benefiting the frequency bandwidth and penetration of ultrasonic transducers. This work highlights the crucial role of phase-field simulations in guiding the design of Sm-doped PMN-PT ceramics and crystals to achieve record-high piezoelectricity.

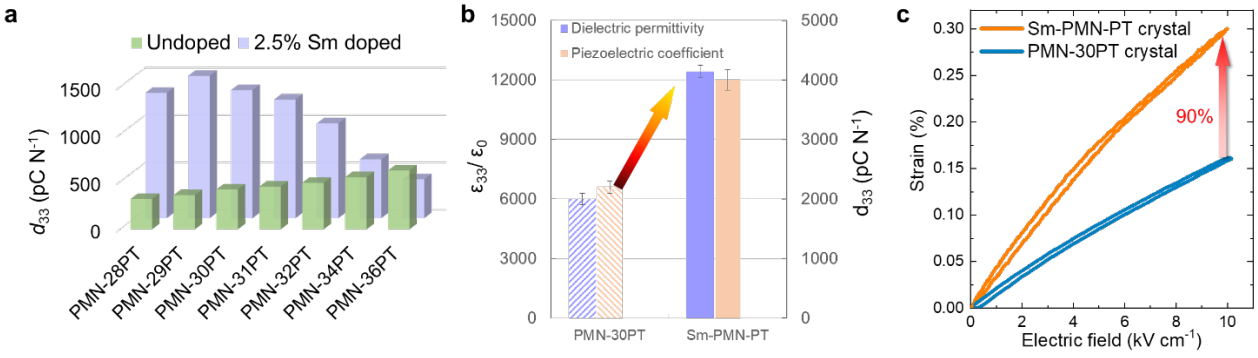

Figure 6 (a) The piezoelectric coefficient d_{33} of 2.5 mol% Sm-doped PMN–xPT and undoped PMN–xPT ceramics. (b) The piezoelectric coefficient d_{33} of [001]-oriented Sm-doped PMN–30PT and undoped PMN–30PT crystals, measured using a Berlincourt d_{33}-meter. (c) Electric-field-induced strain for Sm-doped PMN–30PT and undoped PMN–30PT crystals. The data is from references 17 and 18.

Discovery of unprecedented transparency of relaxor ferroelectric crystals with ultrahigh

piezoelectricity

It was first reported by Yamashita et al. in 2011[40] that the piezoelectric property of rhombohedral relaxor-PT crystals could be improved by 20~100% via poling with an a.c. electric field instead of the conventionally used d.c. electric field (see a recent review[41]). It was believed that the piezoelectricity enhancement through a.c.-poling is due to increased domain wall density[42] since there is a general belief in the community that the smaller the domain size, the higher the piezoelectricity.[43-44] However, it has been challenging to experimentally characterize and analyze the domain structure evolution during a.c. and d.c. poling, and thus the attribution of the enhanced piezoelectricity of a.c. poled crystals to the reduction of domain size or increase in domain wall density had been speculative.

We performed phase-field simulations to analyze the dynamical evolution of the ferroelectric polarization and domain structure of the relaxor-PT crystals subject to the direct or alternating electric fields. We considered a rhombohedral relaxor-PT crystal, and thus the unpoled domain structure consists of eight domain variants and has zero net polarization (**Fig. 7a**)[23]. After poling with a d.c. electric field along $[001]_{pc}$, four of the eight domain variants that have out-of-plane polarization antiparallel to the external electric field direction are switched to the other four domain variants, forming a laminated domain structure, as shown in Fig. 7b. The horizontal layers are separated by a set of 109° domain walls parallel to the $(001)_{pc}$ plane, while within each lamina, there are inclined 71° domain walls approximately parallel to the $\{011\}_{pc}$ planes. When the applied electric field is reversed for several cycles to mimic the a.c. poling process, the 71° domain walls tend to re-orient between the $(011)_{pc}$ and $(01\bar{1})_{pc}$ planes via the nucleation and growth of the opposite domain variants. As a result, a pair of neighboring 71° domain walls tend to merge, and the density of 71° domain wall within a layer decreases, which can be fully eliminated under stress-free conditions as shown in Fig. 7c. In contrast, most of the horizontal 109° domain walls remain still during the process. The animations of the simulated domain structure evolution subjected to a.c. and d.c. electric fields can be found in Ref. 23.

Therefore, in contrast to the general belief that a.c. poling reduced domain size, our phase-field simulations demonstrated the overall domain size in the a.c.-poled crystals is larger than those obtained in d.c.-poling. The predictions on the domain morphology and domain size dependence on poling conditions are later successfully verified by a range of experiments, including scanning electron microscopy (Fig. 7d), birefringence imaging microscopy[23], and synchrotron X-ray diffraction[45].

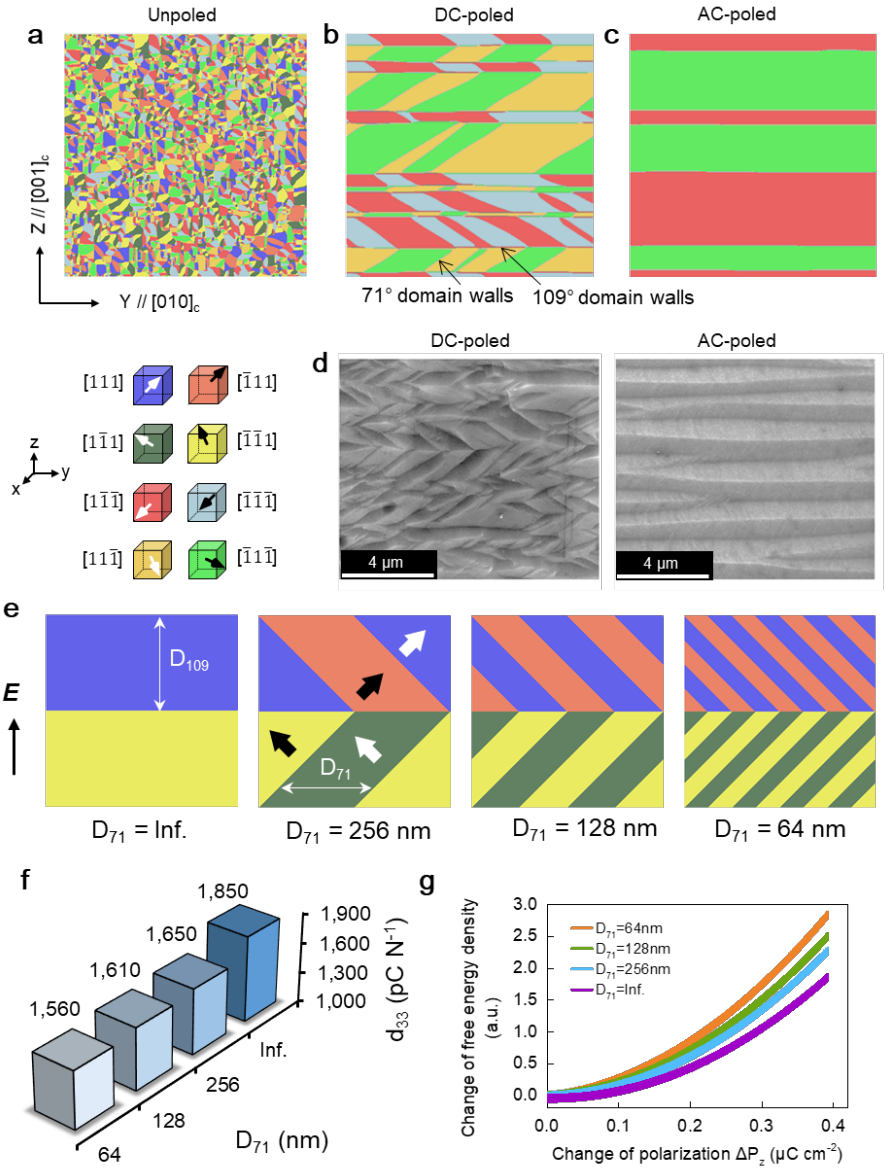

Figure 7 Phase-field simulation of 2D domain structures of rhombohedral PMN-28PT crystals at equilibrium of (a) unpoled, (b) d.c.-poled, and (c) a.c.-poled under stress-free conditions. The poling direction is along $[001]_{pc}$. The colors of domains correspond to the eight domain variants with polarization along $<111>_{pc}$ directions as denoted in the legend below (a). (d) SEM images of cross-sections of a.c.-and d.c.-poled PMN-28PT crystals. (e) Schematics of the layered 4R domain structures of [001]-poled PMN-28PT with varied widths of the 71° domains (D_{71}). D_{71} = Inf. means no 71° domain walls are present in the system. (f) Calculated d_{33} along [001] direction of the corresponding domain configurations in (e) as a function of D_{71}. (g) The free energy landscape of the system with respect to ΔP_z. The free-energy densities of each case are normalized with respect to the $\Delta P_z = 0$ state. (a-c) and (e-g) adapted with permission from Reference 23 © 2020 Springer Nature.

To understand the domain size effect on piezoelectricity of the [001]-poled relaxor-PT, we performed

phase-field simulations to systematically evaluate the relationship between the domain size and the piezoelectric coefficient of the layered structures with controlled density of the 71° domain walls (Fig. 7e). Remarkably, the a.c.-poled crystal with reduced density of 71° domain walls shows higher piezoelectric coefficient than their d.c.-poled counterpart, in stark contrast to the general belief that small domain sizes favor high piezoelectricity (Fig. 7f). As a matter of fact, our further thermodynamic analysis and phase-field simulations demonstrate that the inverse domain size effect (i.e., larger domain size gives higher piezoelectricity) is more common than expected[46]. Specifically, the nature of the domain-size dependence of piezoelectricity is shown to be determined by the variation of piezoelectricity inside the domains instead of the domain wall contributions[46], and the domain size effect can be tuned via several approaches.[47-49] In the case of [001]-poled rhombohedral relaxor-PT crystals, the reduced 71° domain wall density flattens the free energy profile (Fig. 7g), thus facilitates the polarization rotation process of the ferroelectric domains and leads to increased piezoelectricity of the crystal.[23,46]

The phase-field predicted layer domain structures with the layers separated by mostly parallel 109° domain walls normal to the poling direction and the 71° domain walls within the layers eliminated by the a.c. poling provide important clues about the possible high transparency of the a.c. poled crystals. While the 71° domain walls are light-scattering, the 109° domain walls are not light-scattering based on the optical indicatrices of the neighboring domains within the domain structures.[23] Therefore, it is expected that the optical and electrooptical properties of the a.c.-poled relaxor-PT crystals should also be enhanced compared with the d.c.-poled samples because of the elimination of the light-scattering 71° domain walls in the normal incident direction (i.e., $[001]_{pc}$).[23] Indeed, careful polishing of the crystal surfaces of the a.c.-poled PMN-PT rhombohedral crystal reveals high optical transparency as confirmed by the light transmittance spectrum and the apparent transparent appearance of the crystal, as shown in **Fig. 8**. Furthermore, the birefringence and the electrooptical coefficients of the a.c.-poled relaxor-PT have been significantly enhanced.[23]

This example highlights not only the roles of phase-field simulations in understanding the universal relationship between the engineered domain structures and overall effective piezoelectric properties but also in the discovery of simultaneous high light-transparency and piezoelectricity of a.c. poled crystals.

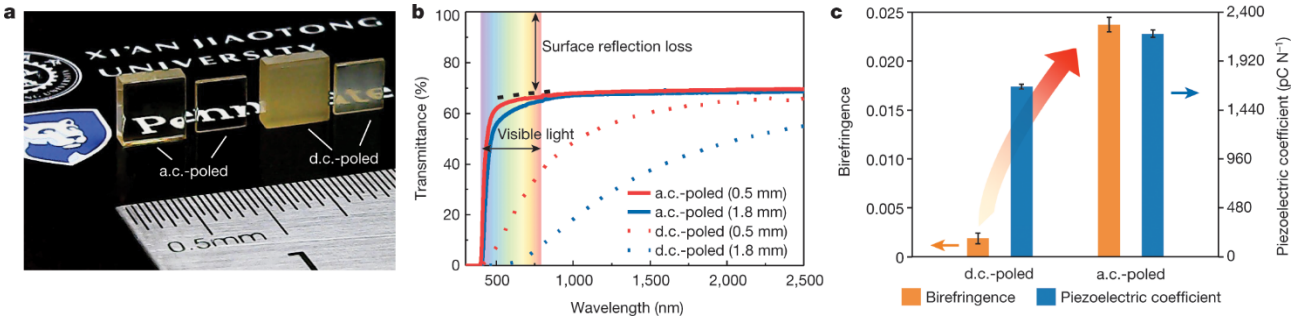

Figure 8 (a) Photograph of a.c- and d.c.-poled PMN-28PT crystals. The thicknesses of the crystals are 0.5 mm and 1.8 mm, respectively. (b) Light transmittance of the a.c.- and d.c.-poled PMN-28PT crystals. (c) d_{33} and birefringence of the a.c.- and d.c.-poled PMN-28PT crystals. (a-c) adapted with permission from Reference 23 © 2020 Springer Nature.

Impacts of high-performance piezoelectric materials enabled by phase-field modeling-guided design

The development of Sm-doped PMN-PT with record-high piezoelectricity and the discovery of transparent ultrahigh piezoelectric crystals have not only advanced the fundamental understanding of ferroelectric materials but also led to patents that spur broader technology interests[50,51]. Based on these new relaxor ferroelectric materials, several high-performance electromechanical and electro-optical devices have been developed, as highlighted in **Fig. 9**. For example, by using the Sm-doped PMN-PT ceramics to replace conventional PZT ceramics, the output acoustic pressure of a 2D array ultrasonic transducer was doubled, showing a great promising for low-intensity ultrasound therapy applications[26]. Using Sm-doped PMN-PT crystals, an implanted energy harvester was fabricated with ultrahigh output power density, thus can immediately activate the periaqueductal gray brain area and qualified for deep brain stimulation and analgesia applications[28]. Dagdeviren's group at MIT developed several new conformable ultrasound patches by using rare-earth doped relaxor ferroelectric crystals and ceramics, showing sufficient contrast sensitivity and desired axial/lateral resolution for soft tissue imaging[30,31]. Owing to the ultrahigh electro-optic coefficients in transparent relaxor ferroelectric crystals, Liu et al. designed a new compact electro-optical *Q*-switch, whose volume and driving voltage were substantially reduced by around one order of magnitude when compared with commercial $LiNbO_3$ and deuterated potassium dihydrogen phosphate(DKDP)-based *Q*-switches[52]. Benefiting from the ultrahigh piezoelectricity, relaxor ferroelectric crystals also showed great effectiveness in miniaturizing the piezoelectric motors with high moving resolution[53]. Taking the advantages of simultaneously possessing high light-transmission and large piezoelectricity, several new transparent electromechanical devices were also designed, such as transparent millirobots[29], transparent ultrasonic transducers for photoacoustic imaging and transparent piezoelectric metasurfaces for adaptive optics[54].

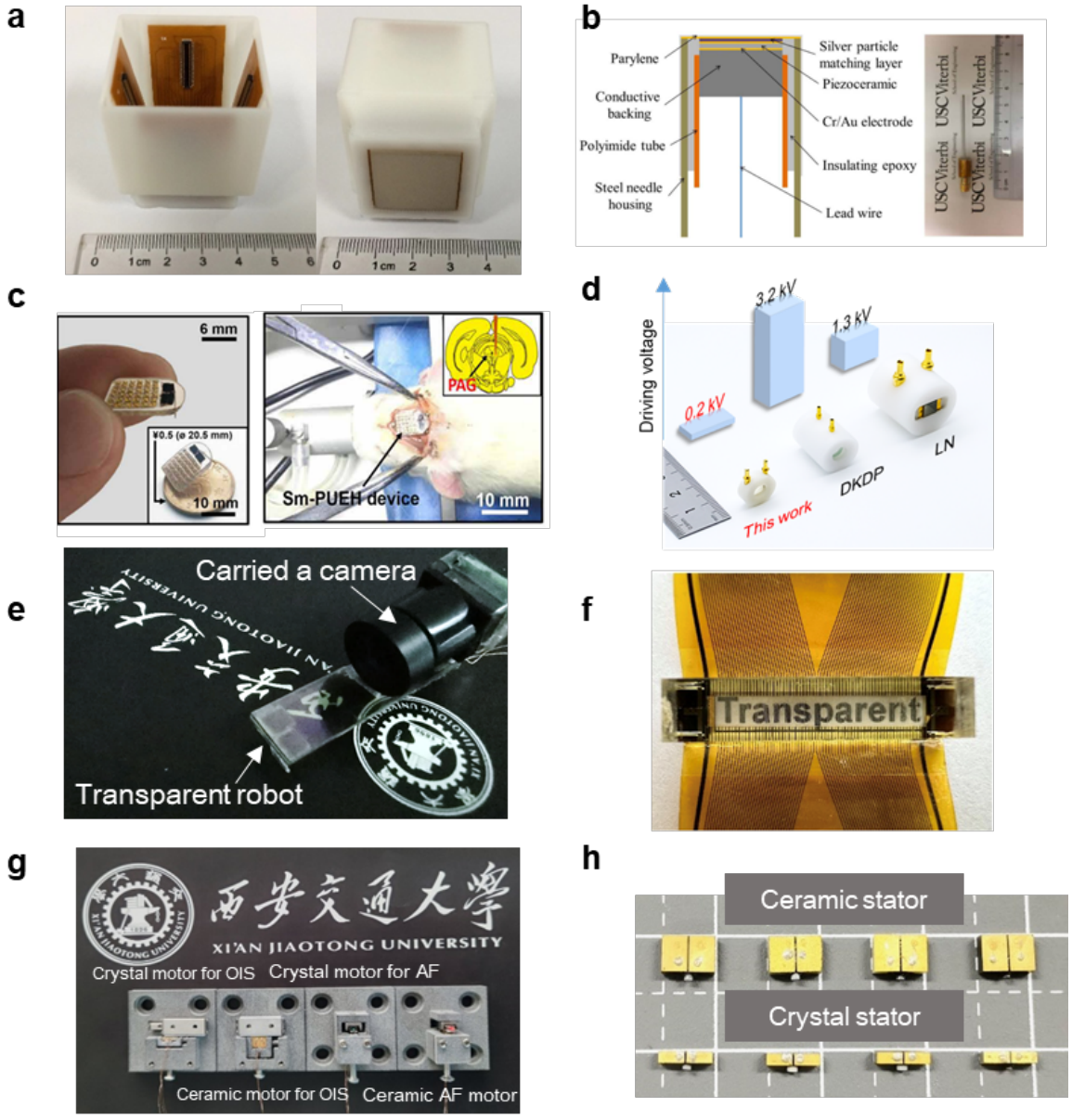

Figure 9 Recently developed devices based on high-performance relaxor ferroelectric single crystals and ceramics. (a) 2-D transducer array for ultrasound therapy application based on Sm-doped PMN-PT ceramics, from Ref. 26; (b) high-frequency needle transducer, from Ref. 27; (c) flexible energy–harvesting device for deep brain stimulation, from Ref. 28; (d) electro-optic *Q*-switches based on transparent relaxor ferroelectric crystals, from Ref. 52; (e) a transparent millirobot based on transparent relaxor ferroelectric crystals, from Ref. 29; (f) a transparent ultrasonic transducer array based on transparent relaxor ferroelectric crystals for photoacoustic imaging; (g) piezoelectric motors based on relaxor ferroelectric crystal and PZT ceramic, from Ref. 53; (h) stator components of piezoelectric motors, showing the effectiveness of relaxor ferroelectric crystals in miniaturization of motors. (a-e) adapted with permission from Reference 26 © 2020 IEEE, Reference 27 © 2017 IEEE, Reference 28 © 2022 AAAS, Reference 52 © 2022 AAAS, Reference 29 © 2022 AIP.

Summary and Outlook

In this article, we demonstrate the unique capability of phase-field modeling in unveiling the fundamental mesoscale mechanisms of ferroelectric domain evolution piezoelectricity and guiding the design of advanced relaxor ferroelectric crystals for piezoelectric applications. Specifically, phase-field simulation help us understand the relationship between multiscale microstructures and macroscopic properties of relaxor ferroelectrics, thus accelerating the design of a series of rare earth element doped relaxor ferroelectric ceramics and crystals with greatly enhanced piezoelectricity[17-20], as well as the discovery of transparent relaxor ferroelectric crystals with ultrahigh piezoelectric and electrooptic properties[23,52,55]. These high-performance piezoelectric materials have enabled or stimulated a number of device applications that would be otherwise challenging or restricted by the inadequate properties of the prevailing piezoelectric materials. We highlighted a few such device applications that are currently being extensively explored by many around the world, which are expected to produce more comfortable and higher fidelity medical ultrasonography[26,27,30,31], flexible energy harvesting with higher efficiency[28,56], and further miniaturized transparent robotics[29]. We believe many of these lab-scale prototypes hold substantial promises for mass production and commercialization in the near future.

In addition to the demonstrated success in advancing the research on relaxor ferroelectric crystals, the phase-field method can also be employed to guide the understanding and design of other ferroelectric and related materials and the discovery of new mesoscale phenomena. Examples include solid-state refrigeration utilizing the multi-caloric effects of ferroic materials[57], flexible electronics based on polymer-ceramic nanocomposites[58], high energy-density storage using advanced dielectric materials[59, 60], multifunctional devices enabled by multiferroic magnetoelectric heterostructures[61], textured ceramics[62, 63] among others. There are also new opportunities that can potentially benefit from employing the phase-field approach to tackle the fundamental materials problems and create broader impacts. For example, how to mitigate the wake-up and fatigue issues of HfO_2-based ferroelectric materials is critical for developing robust CMOS-compatible ferroelectric devices for neuro-inspired computing[64,65], while a comprehensive phase-field model can help elucidate the thermodynamic and kinetic factors underpinning the phase transitions and polarization switching during these processes. We expect that the ever-developing advanced numerical computation algorithms, machine-learning models, and data-driven methods, such as GPU-accelerated algorithms [66], physics-informed neutral networks[67,68], machine-learned interatomic potentials[69] and machine-learned free energies[70], can be employed further to accelerate the formulation, parametrization and computation of phase-field models for the new materials systems and ultimately lead to breakthroughs

in broader fields.

Authors Contributions

F.L. and B.W. write the manuscript. L.Q.C. revised the manuscript. All the authors discussed the content of the manuscript.

Funding

F. Li acknowledgement financial support from the National Natural Science Foundation of China (Grant No. 52325205). Part of this work was performed under the auspices of the U.S. Department of Energy by Lawrence Livermore National Laboratory under Contract DE-AC52-07NA27344 (B.W.). The effort at Penn State is supported by the National Science Foundation (NSF) through Grant No. DMR- 2133373 and DMR-1744213.

Competing interests

The authors declare that they have no competing interests.

References:

1. G. A. Smolenskii, N.N. Krainik, A.A. Berezhnoi, *Solid State Phys.* **10**, 2675 (1968).
2. Y. Yokomizo, T. Takahashi, S. Nomura, *J. Phys. Soc. Jpn*. **28**, 1278 (2007).
3. J. Kuwata, K. Uchino, S. Nomura, *Jpn.J.Appl.Phys.* **21**, 1298 (1982).
4. S.-E. Park, T.R. Shrout, *J. Appl. Phys.* **82**, 1804 (1997).
5. H. Luo, G. Xu, P. Wang, Z. Yin, *Ferroelectrics* **231**, 97 (1999).
6. S. Zhang, F. Li, *J. Appl. Phys.* **111** (2012).
7. Z.-G. Ye, *MRS Bull.* **34**, 277 (2009).
8. E. Sun, W. Cao, *Prog. Mater. Sci.* **65**, 124 (2014).
9. D. Damjanovic, *IEEE Trans. Ultrason., Ferroelectr., Freq. Control* **56**, 1574 (2009).
10. H. Fu, R.E. Cohen, *Nature* **403**, 281 (2000).
11. B. Noheda, *Curr. Opin. Solid State Mater. Sci.* **6**, 27 (2002).
12. Z. Kutnjak, J. Petzelt, R. Blinc, *Nature* **441**, 956 (2006).
13. G. Xu, J. Wen, C. Stock, P. Gehring, *Nat. Mater.* **7**, 562 (2008).
14. D. Phelan, C. Stock, J.A. Rodriguez-Rivera, S. Chi, J. Leão, X. Long, Y. Xie, A.A. Bokov, Z.-G. Ye, P. Ganesh, *Proc. Natl. Acad. Sci.* **111**, 1754 (2014).
15. Y. Jin, Y.U. Wang, A.G. Khachaturyan, J. Li, D. Viehland, *Phys. Rev. Lett.* **91**, 197601 (2003).
16. S. Zhang, F. Li, X. Jiang, J. Kim, J. Luo, X. Geng, *Prog. Mater. Sci.* **68**, 1 (2015).
17. F. Li, M.J. Cabral, B. Xu, Z. Cheng, E.C. Dickey, J.M. LeBeau, J. Wang, J. Luo, S. Taylor, W. Hackenberger, *Science* **364**, 264 (2019).
18. F. Li, D. Lin, Z. Chen, Z. Cheng, J. Wang, C. Li, Z. Xu, Q. Huang, X. Liao, L.-Q. Chen, *Nat. Mater.* **17**, 349 (2018).
19. Q. Li, Y. Liu, J. Liu, K. Song, H. Guo, F. Li, Z. Xu, *Adv. Funct. Mater.* **32**, 2201719 (2022).
20. Y. Liu, Q. Li, L. Qiao, Z. Xu, F. Li, *Adv. Sci.* **9**, 2204631 (2022).
21. F. Li, S. Zhang, T. Yang, Z. Xu, N. Zhang, G. Liu, J. Wang, J. Wang, Z. Cheng, Z.-G. Ye, *Nat. Commun.* **7**, 13807 (2016).
22. F. Li, S. Zhang, Z. Xu, L.Q. Chen, *Adv. Funct. Mater.* **27**, 1700310 (2017).
23. C. Qiu, B. Wang, N. Zhang, S. Zhang, J. Liu, D. Walker, Y. Wang, H. Tian, T.R. Shrout, Z. Xu, *Nature* **577**, 350 (2020).
24. H. Wan, C. Luo, C. Liu, W.-Y. Chang, Y. Yamashita, X. Jiang, *Acta Mater.* **208**, 116759 (2021).
25. H.-P. Kim, H. Wan, C. Luo, Y. Sun, Y. Yamashita, T. Karaki, H.-Y. Lee, X. Jiang, *IEEE Trans. Ultrason., Ferroelectr., Freq. Control* (2022).
26. Z. Zhang, M. Su, F. Li, R. Liu, R. Cai, G. Li, Q. Jiang, H. Zhong, T.R. Shrout, S. Zhang, *IEEE Trans. Ultrason., Ferroelectr., Freq. Control* **67**, 2085 (2020).
27. Z. Zhang, F. Li, R. Chen, T. Zhang, X. Cao, S. Zhang, T.R. Shrout, H. Zheng, K.K. Shung, M.S. Humayun, *IEEE Trans. Ultrason., Ferroelectr., Freq. Control* **65**, 223 (2017).
28. T. Zhang, H. Liang, Z. Wang, C. Qiu, Y.B. Peng, X. Zhu, J. Li, X. Ge, J. Xu, X. Huang, *Sci. Adv.* **8**, eabk0159 (2022).
29. X. Gao, L. Qiao, C. Qiu, T. Wang, L. Zhang, J. Liu, S. Yang, H. Jin, B. Xin, S. Zhang, *Appl. Phys. Lett.* **120,** 032902 (2022).
30. L. Zhang, C. Marcus, D. Lin, D. Mejorado, S. J. Schoen Jr, T. T. Pierce, V. Kumar, S. V. Fernandez, D. Hunt, Q. Li, I. I. Shuvo, D. Sadat, W. Du, H. Edenbaum, L. Jin, W. Liu, Y. C. Eldar, F. Li, A. P. Chandrakasan, A. E. Samir, C. Dagdeviren, *Nat. Electron.* **7,** 77–90 (2024).
31. W. Du, L. Zhang, E. Suh, D. Lin, C. Marcus, L. Ozkan, A. Ahuja, S. Fernandez, I.I. Shuvo, D.

Sadat, *Sci. Adv.* **9**, eadh5325 (2023).
32. J. Wang, B. Wang, L.Q. Chen, *Annual Rev. Mater. Res.*, **49**, 127–52 (2019).
33. L.Q. Chen, *J. Am. Ceram. Soc.*, **91**, 1835–44 (2008).
34. D. Schrade, R. Müller, D. Gross, *Arch. Appl. Mech.*, **83**, 1393–1413 (2013).
35. A. Bokov, Z.-G. Ye, *J. Mater. Sci.* **41**, 31 (2006).
36. F. Li, S. Zhang, D. Damjanovic, L.Q. Chen, T.R. Shrout, *Adv. Funct. Mater.* **28**, 1801504 (2018).
37. M.E. Manley, D.L. Abernathy, R. Sahul, D.E. Parshall, J.W. Lynn, A.D. Christianson, P.J. Stonaha, E.D. Specht, J.D. Budai, *Sci. Adv.* **2**, e1501814 (2016).
38. G. Xu, G. Shirane, J. Copley, P. Gehring, *Phys. Rev. B* **69**, 064112 (2004).
39. J. Chen, H.M. Chan, M.P. Harmer, *J. Am. Ceram. Soc.* **72**, 593 (1989).
40. Y. Yamashita, N. Yamamoto, Y. Hosono, K. Itsumi, *US Patent* 2015/0372219 A1 (2015).
41. H.-P. Kim, H. Wan, C. Luo, Y. Sun, Y. Yamashita, T. Karaki, H.-Y. Lee, X. Jiang, *IEEE Trans. Ultrason., Ferroelectr., Freq. Control* **69**, 3037 (2022).
42. J. Xu, H. Deng, Z. Zeng, Z. Zhang, K. Zhao, J. Chen, N. Nakamori, F. Wang, J. Ma, X. Li, H. Luo, *Appl. Phys. Lett.* **112**, 182901 (2018).
43. G. Arlt, D. Hennings, G. De With, *J. Appl. Phys*., **58**, 1619 (1985).
44. S. Wada, K. Yako, H. Kakemoto, T. Tsurumi, T. Kiguchi, *J. Appl. Phys*., **98**, 014109 (2005).
45. C. Qiu, Z. Xu, Z. An, J. Liu, G. Zhang, S. Zhang, L.Q. Chen, N. Zhang, F. Li, *Acta Mater.*, **210**, 116853 (2021).
46. B. Wang, F. Li, L.Q. Chen, *Adv. Mater.* **33**, 2105071 (2021).
47. P. Ondrejkovic, P. Marton, M. Guennou, N. Setter, J. Hlinka, *Phys. Rev. B* **88**, 024114 (2013).
48. T. Sluka, A.K. Tagantsev, D. Damjanovic, M. Gureev, N. Setter, *Nat. Commun.* **3**, 748 (2012).
49. J. Hlinka, P. Ondrejkovic, P. Marton, *Nanotechnology* **20**, 105709 (2009).
50. F. Li, D. Lin, S. Zhang, T. R. Shrout, L.Q. Chen. US Patent, US 10,811,593 B2 (Oct. 20, 2020).
51. F. Li, C. Qiu, Z. Xu, B. Wang, L.Q. Chen, S. Zhang, T. R. Shrout. US Patent 11,758,818 (Sep. 12, 2023).
52. X. Liu, P. Tan, X. Ma, D. Wang, X. Jin, Y. Liu, B. Xu, L. Qiao, C. Qiu, B. Wang, *Science* **376**, 371 (2022).
53. J. Liu, X. Gao, H. Jin, K. Ren, J. Guo, L. Qiao, C. Qiu, W. Chen, Y. He, S. Dong, *Nat. Commun.* **13**, 6567 (2022).
54. L. Qiao, X. Gao, K. Ren, C. Qiu, J. Liu, H. Jin, S. Dong, Z. Xu, F. Li, *Nat. Commun.* **15**, 805 (2024).
55. C. Deng et al., *Adv. Mater*. **33**, e2103013 (2021).
56. N. Jia, Q. Li, C. Li, H. Du, X, Gao, Y. Liu, K. Song, H. Jin, K. Ren, C. Qiu, L. Ning, Z. Xu, F. Li, *Energy Environ. Sci.*, https://doi.org/10.1039/D3EE03168C2024 (2024)
57. R. Gao, X. Shi, J. Wang, H. Huang, *J. Am. Ceram. Soc.* **105**, 3689 (2022).
58. Z.-H. Shen, T.-X. Tang, J. Wang, M.-J. Zhou, H.-X. Liu, L.-Q. Chen, Y. Shen, C.-W. Nan, *Nano Energy* **117**, 108933 (2023).
59. B. Yang, Q. Zhang, H. Huang, H. Pan, W. Zhu, F. Meng, S. Lan, Y. Liu, B. Wei, Y. Liu, *Nat. Energy* **8**, 956 (2023).
60. Z.H. Shen, J.J. Wang, Y. Lin, C.W. Nan, L.Q. Chen, Y. Shen:, *Adv. Mater.* **30**, 1704380 (2018).
61. J.-M. Hu, C.-G. Duan, C.-W. Nan, L.-Q. Chen, *npj Comput. Mater.* **3**, 18 (2017).
62. C. Ming, T. Yang, K. Luan, L. Chen, L. Wang, J. Zeng, Y. Li, W. Zhang, L.-Q. Chen, *Acta Mater.* **145**, 62 (2018).

63. J. Li, W. Qu, J. Daniels, H. Wu, L. Liu, J. Wu, M. Wang, S. Checchia, S. Yang, H. Lei, R. Lv, Y.. Zhang, D. Wang, X. Li, X. Ding, J. Sun, Z. Xu, Y. Chang, S. Zhang, F. Li, *Science* **380**, 87 (2023).
64. B. Noheda, P. Nukala, M. Acuautla, *Nat. Mater.* **22**, 562 (2023).
65. U. Schroeder, M.H. Park, T. Mikolajick, C.S. Hwang, *Nat. Rev. Mater.* **7**, 653 (2022).
66. P. Kumar, A. Nonaka, R. Jambunathan, G. Pahwa, S. Salahuddin, Z. Yao, *Comput. Phys. Commun.* **290**, 108757 (2023).
67. W. Li, M.Z. Bazant, J. Zhu, *arXiv preprint arXiv:2302.13368* (2023).
68. C.L. Wight, J. Zhao, *arXiv preprint arXiv:2007.04542* (2020).
69. J. Wu, Y. Zhang, L. Zhang, S. Liu, *Phys. Rev. B* **103**, 024108 (2021).
70. G.H. Teichert, A.R. Natarajan, A. Van der Ven, K. Garikipati, *Comput. Method Appl. M.* **353**, 201 (2019).